Acta Materialia 247 (2023) 118734

Contents lists available at ScienceDirect

Acta Materialia

journal homepage: www.elsevier.com/locate/actamat

Full length article

Calculation of dislocation binding to helium-vacancy defects in tungsten using hybrid ab initio-machine learning methods

Petr Grigorev [*,a], Alexandra M. Goryaeva [b], Mihai-Cosmin Marinica [b], James R. Kermode [c], Thomas D. Swinburne [a]

[a] Aix-Marseille Université, CNRS, CINaM UMR 7325, Campus de Luminy, Marseille 13288, France
[b] Université Paris-Saclay, CEA, Service de recherche en Corrosion et Comportement des Matériaux, SRMP, 91191, Gif-sur-Yvette, France
[c] Warwick Centre for Predictive Modelling, School of Engineering, University of Warwick, Coventry CV4 7AL, UK

ARTICLE INFO

Keywords:
Plasticity
Dislocations
Tungsten
Helium
Segregation
Density functional theory
QM/MM
Machine learning

ABSTRACT

Calculations of dislocation-defect interactions are essential to model metallic strength, but the required system sizes are at or beyond ab initio limits. Current estimates thus have extrapolation or finite size errors that are very challenging to quantify. Hybrid methods offer a solution, embedding small ab initio simulations in an empirical medium. However, current implementations can only match mild elastic deformations at the ab initio boundary. We describe a robust method to employ linear-in-descriptor machine learning potentials as a highly flexible embedding medium, precisely matching dislocation migration pathways whilst keeping at least the elastic properties constant. This advanced coupling allows dislocations to cross the ab initio boundary in fully three dimensional defect geometries. Investigating helium and vacancy segregation to edge and screw dislocations in tungsten, we find long-range relaxations qualitatively change impurity-induced core reconstructions compared to those in short periodic supercells, even when multiple helium atoms are present. We also show that helium-vacancy complexes, considered to be the dominant configuration at low temperatures, have only a very weak binding to screw dislocations. These results are discussed in the context of recent experimental and theoretical studies. More generally, our approach opens a vast range of mechanisms to ab initio investigation and provides new reference data to both validate and improve interatomic potentials.

1. Introduction

Dislocations are extended line defects which carry plastic deformation in crystalline materials [1]. Dislocation motion is impeded by point defects such as vacancies or impurity atoms; these can either be static obstacles or diffusing defects attracted by the dislocation's long range elastic field [2–8].

A quantitative and mechanistic understanding of point-defect dislocation interactions is therefore of primary importance to build accurate models for rational alloy design strategies [7], or to predict and mitigate the risk of catastrophic brittle failure during service under hostile conditions [9]. For this task, ab initio calculations, specifically density functional theory (DFT) [10], are essential to capture dislocation core structures and complex bonding to impurity elements. However, the computational cost of DFT typically scales as $\mathcal{O}(N^3)$ for metallic systems, which severely limits its direct applicability to the study of extended defects (Section 2.1). As a result, dislocation-impurity studies remain challenging or approximate, requiring resources at or beyond the limits of many practitioners, essentially ruling out the systematic studies required for rational design approaches.

In this paper, we present and apply a new hybrid simulation method (Section 2) that embeds ab initio simulations in much more general simulation geometries than previously possible, using custom-fit machine learning interatomic potentials [11] (Section 2.2). An open source implementation employing the popular atomic simulation environment (ASE) package [12] is freely available online [13].

The presented method is applied to study the interaction between dislocations and helium-vacancy defects in tungsten (Section 3), a problem of critical importance to the operational stability of future fusion reactors, which are expected to attain helium concentrations of 20 appm after 5 years of operation [14]. Experiment with much higher concentrations, up to 20 atomic %, demonstrate key role of TEM invisible He and He-vacancy clusters in the resulting hardening [15]. Recent large scale MD simulations [16] of edge and mixed dislocations also

* Corresponding author.
E-mail addresses: petr.grigorev@univ-amu.fr (P. Grigorev), thomas.swinburne@cnrs.fr (T.D. Swinburne).

https://doi.org/10.1016/j.actamat.2023.118734
Received 25 October 2022; Accepted 28 January 2023
Available online 3 February 2023

reported these obstacles offer strong strengthening. Experiments with helium implanted tungsten show that He concentration of 20 appm is sufficient to suppress recrystallization and influence intergranular fracture [17]. However, the role of defect-dislocation interactions at much lower helium concentrations, where bubble formation is limited and Helium is assumed to reside primarily in single, immobile dislocations, is limited by the accuracy of available interatomic potentials [18], and remains a largely open question.

The present work provides first ab initio data for the intrinsic properties of ⟨100⟩ edge dislocations and the binding of vacancy and helium defects to both edge and screw dislocations.

Our central results are a) ab initio Peierls barriers for ⟨100⟩ edge dislocations have much less variation with slip plane compared to current interatomic potentials (Section 3.1) b) Non-periodic simulations reveal He induces a reconstruction of the screw dislocation core to the 'split' configuration, unlike the 'hard' configuration found for other impurities [19] (Section 3.4), which suggests a weaker strengthening effect of helium alone. c) helium-vacancy defects have a much weaker binding to screw dislocations (0.3 eV) than vacancies alone (1.2 eV), whilst highly mobile helium interstitials are predicted to have a mild segregation to screw dislocations at fusion-relevant temperatures (Section 3.5), meaning they can only provide an obstacle, rather than pinning, dislocation motion. More generally, we demonstrate our embedding approach can systematically improve Linear Machine Learning (LML) potentials for dislocation simulation, as demonstrated for dislocation-vacancy interactions (Section 3.2). Future directions are discussed in Section 4.

2. Methodology

2.1. Ab initio studies of dislocations

In certain special cases, when the dislocation core is sufficiently compact and the elastic field sufficiently weak, it is possible to contain specialised dislocation multipole configurations in small periodic DFT supercells [20–22]. Whilst simulations of this kind have given significant insight into the nature of intrinsic lattice resistance in a variety of systems [23–25], extending the same methodology to dislocations with large prismatic components is extremely challenging due to the system sizes required to mitigate the resulting strong elastic interactions. The requirement of periodicity along the line direction makes studies of impurity segregation similarly expensive, even with amenable dislocations, due to long ranged core reconstructions as we show below. Recent studies have simulated well over a thousand DFT atoms to infer the converged structure [26].

An alternative to fully periodic supercells is a cluster approach [20, 27–30], where periodicity is kept only along the line of the dislocation (or other extended defects, such as a crack [31]) with free boundary conditions used in other directions. The ab initio region is then coupled to an elastic medium via lattice Green's functions [27] or in the hybrid approach developed here, embedded in an atomistic simulation governed by an interatomic potential [32]. Current hybrid methods still require that deformations remain in the elastic regime at the ab initio boundary [33], meaning dislocations are limited to short, periodic line segments. The methodological developments in this study use a flexible class of interatomic potentials, discussed below, to allow for much more general deformations at the ab initio boundary.

2.2. Linear machine learning (LML) interatomic potentials

The development of interatomic potentials have been revolutionised by the availability of high-dimensional regression algorithms from the machine learning (ML) community [34–36]. We refer the reader to a number of excellent recent reviews in this rapidly growing field [37–41], which has attracted explosive interest [11,42–53]. In the present work we employ the linear machine learning (LML) potential approach [11,45,46,48,51], which has cohesive energy and gradient forces

$$\mathscr{V}^{\mathrm{LML}}(\mathbf{X}) = \mathbf{D}(\mathbf{X})\cdot\boldsymbol{\Theta}, \quad \mathbf{F}^{\mathrm{LML}}(\mathbf{X}) = -\nabla\mathbf{D}(\mathbf{X})\boldsymbol{\Theta}, \tag{1}$$

where the vector $\boldsymbol{\Theta} \in \mathbb{R}^{N_D}$ contains all potential parameters that will be varied, whilst $\mathbf{D}(\mathbf{X}) \in \mathbb{R}^{N_D}$ is a *descriptor vector* of the atomic coordinates $\mathbf{X} \in \mathbb{R}^{3N}$. We calculate descriptors using the `MILADY` simulation package [54], coupled to `LAMMPS` [55]; we also provide a standalone `LAMMPS` implementation. Specific details on the descriptors employed are presented in Appendix C, though our method is general to any LML implementation [47,51].

2.3. Force coupled hybrid QM/ML simulations

Following previous work [32,33,56] we use an 'abrupt force mixing' scheme to couple the ab initio (QM) region to the atomistic simulation, simply taking the ionic forces from each region. The QM simulation has both the desired atomic region of the main simulation and an additional 'buffer' of surrounding atoms to provide the correct electronic environment for the region of interest. Whilst a total energy cannot be rigorously defined in cluster approaches, access to the ionic forces allows energy differences to be calculated via the principle of virtual work, which have been validated against total energy calculations in previous works [33,56] (Appendix A). Total cluster energy differences can be used to provide good approximations to energy differences when surface charge states have limited variation [30], which we validate in Section 3.

Our starting point is thus a 'disk' geometry perpendicular to the simulation line, illustrated on the left part of Fig. 1. Periodic boundary conditions are applied in the directions along the dislocation line while free boundary conditions are used in other two directions. This geometry has been used in all previous works [32,33,56] as any potential with matched elastic and lattice properties is an admissible embedding medium. The thickness of the disk is typically kept to be one translation length along the dislocation line. Here, we use an appropriate linear-in-descriptor ML (LML) potential with a vector of parameters Θ_0; these simulations allow us to obtain ab initio accurate glide barriers and core structures, even for prismatic dislocations that are extremely challenging to contain in periodic ab initio supercells.

To study general dislocation-defect interactions we require a fully three dimensional simulation with significant dislocation line length, to mitigate periodic image interaction along the line. The only geometry which avoids an unfeasibly large QM region is some large simulation cell with a spherical QM region centered on where the defect meets the dislocation core, illustrated on the right port of Fig. 1. Clearly, such '3D' simulations require an embedding potential with precisely matched dislocation core structures *in addition* to the correct elastic properties, allowing the dislocation to cross the hybrid boundary. The next section details how this is achieved by retraining a given LML potential using DFT force data from the initial disk simulation. Details of the DFT implementation used for QM part of the method are given in Appendix B.

2.4. Constrained retraining procedure

Our starting point for retraining is some LML potential (1) with parameters $\boldsymbol{\Theta}_0$ that can closely match at least the DFT lattice and elastic constants; we target an error of less than 1 %. Whilst this is sufficient, in practice we start from a state-of-the-art parametrization [11,54]. Use of an already optimized potential additionally allows us to investigate the effect of our retraining procedure in more detail. As discussed above and shown in Fig. 2(c), using the original potential $\boldsymbol{\Theta}_0$ in QM/ML simulations will produce new ionic forces $\mathbf{F}^{\mathrm{QM/ML}}$ in the cluster region, with associated descriptor gradients $\nabla\mathbf{D}^{\mathrm{QM/ML}}$. Our goal is to find a new

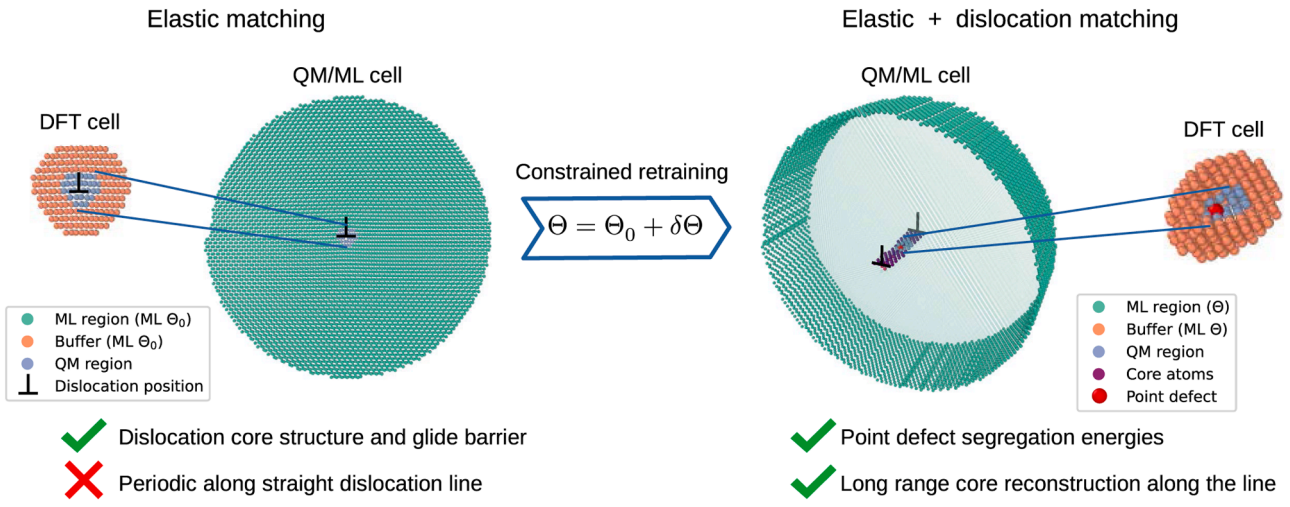

Fig. 1. Left: Standard quasi-2D QM/ML simulations for ab initio accurate dislocation glide barriers, using initial LML parameters $\boldsymbol{\Theta}_0$ with correct elastic properties. Right: Constrained retraining on QM/ML data gives new LML parameters $\boldsymbol{\Theta}$ which additionally have precise matching of target dislocation properties. This allows 3D QM/ML simulations with a spherical QM region at the site of the defect-dislocation interaction.

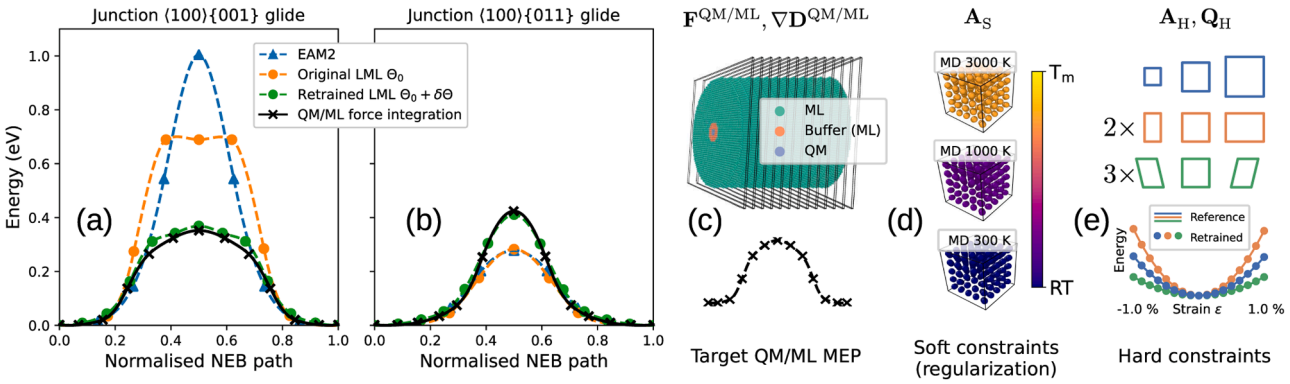

Fig. 2. Peierls barriers of edge (or junction) dislocations with $\mathbf{b} = \langle 100 \rangle$ (a) gliding in {001} and (b) in {011} planes. The barriers are obtained by our NEB method showing the total energy variation along the path for the potentials (dashed lines and dots) and virtual work from force integration for QM/ML results (black solid lines and crosses). (c) An illustration of the QM/ML NEB pathway which the retraining procedure targets. Schematic representations of (d) bulk molecular dynamics snapshots at finite temperatures used to generate 'soft' constraints for regularization and (e) strained bulk configurations used to generate 'hard' constraints for elastic properties.

parametrization $\boldsymbol{\Theta} = \boldsymbol{\Theta}_0 + \delta\boldsymbol{\Theta}$, which minimizes the error to $\mathbf{F}^{\mathrm{QM/ML}}$ whilst *exactly* preserving 'hard' properties such as elastic properties and approximately maintaining 'soft' properties such as forces from high temperature MD that are important to avoid overfitting issues [48].

To define suitable constraints, we note that under weak, arbitrary homogeneous deformations, the total energy change of a lattice is uniquely determined by the elastic constants. As illustrated in Fig. 2(e), we therefore simply subject a perfect lattice (here, bcc) to multiple shear/expansion deformations, collating the energy differences into a vector $\mathbf{t}_{\mathrm{H}} \in \mathbb{R}^{N_{\mathrm{H}}}$, with corresponding descriptor vectors collated into a rectangular 'design matrix' $\mathbf{A}_{\mathrm{H}} \in \mathbb{R}^{\mathrm{N_H} \times \mathrm{N_D}}$. We are free to include additional properties alongside the elastic deformations- for example, in the next section, we also include the structures for vacancy migration. We provide a routine to generate these constraints using the Atomic Simulation Environment [12] (Code Availability). To exactly preserve the hard constraints we require the predicted values $\mathbf{t}_{\mathrm{H}}$ are unchanged, i.e.

$$\mathbf{t}_{\mathrm{H}} \equiv \mathbf{A}_{\mathrm{H}}\boldsymbol{\Theta}_0 = \mathbf{A}_{\mathrm{H}}[\boldsymbol{\Theta}_0 + \delta\boldsymbol{\Theta}], \quad \Rightarrow \mathbf{A}_{\mathrm{H}}\delta\boldsymbol{\Theta} = \mathbf{0}. \tag{2}$$

A solution for $\mathbf{A}_{\mathrm{H}}\delta\boldsymbol{\Theta} = \mathbf{0}$ requires that the rank $\mathrm{R_H} = \mathrm{rank}(\mathbf{A}_{\mathrm{H}})$ is less than the dimension $\mathrm{N_D}$ of $\delta\boldsymbol{\Theta}$. This is a central motivation for using the quadratically extended descriptor formalism, which gives $\mathrm{N_D} \sim 1500$ even when calculating less than a hundred descriptor functions per atom (Appendix C). For this descriptor choice, the elastic constraints alone gave $\mathrm{R_H} = 25$, rising to 37 when including vacancy migration. To find a general solution, we apply singular value decomposition (SVD) [57] to $\mathbf{A}_{\mathrm{H}}$, obtaining $\mathrm{R_H}$ singular values, along with a set of $\mathrm{R_H}$ orthonormal right singular vectors $\mathbf{v}_1, \ldots, \mathbf{v}_{\mathrm{R_H}}$. We note this procedure naturally eliminates any duplication of data when building $\mathbf{A}_{\mathrm{H}}$, meaning it is simple to build constraints for e.g. highly anisotropic elastic properties. Any right vector $\mathbf{w} \in \mathbb{R}^{\mathrm{N_D}}$ that has non-zero projection $\mathbf{A}_{\mathrm{H}}\mathbf{w} \neq \mathbf{0}$ can thus be expressed as a linear combination of the right singular vectors. Forming a projection matrix $\mathbf{P}_{\mathrm{H}} = \sum_m \mathbf{v}_m \mathbf{v}_m^{\top} \in \mathbb{R}^{\mathrm{N_D} \times \mathrm{N_D}}$, A general solution can then be found by forming the *null space* projection matrix $\mathbf{Q}_{\mathrm{H}} = \mathbb{I} - \mathbf{P}_{\mathrm{H}}$, such that $\mathbf{A}_{\mathrm{H}}\mathbf{Q}_{\mathrm{H}}\mathbf{v} = \mathbf{0}$ for *any* vector $\mathbf{v}$. As a result, $\delta\boldsymbol{\Theta} = \mathbf{Q}_{\mathrm{H}}\mathbf{v}$ will always satisfy Eq. (2). In principle, one can then search for the vector $\delta\boldsymbol{\Theta}$ that best matches QM/ML forces, whilst also satisfying $\mathbf{P}_{\mathrm{H}}\delta\boldsymbol{\Theta} = \mathbf{0}$. However, as $\mathrm{R_H} \ll \mathrm{N_D}$, in practice, this regression procedure is vulnerable to overfitting. To correct for this, we additionally require that the new refitted potential approximately preserves a set of properties of the original potential, to provide further 'soft' constraints. We have found that including molecular dynamics trajectories of the bulk crystal at a range of temperatures (Fig. 2(d)) gives a 'soft' targets $\mathbf{t}_{\mathrm{S}}$ and design matrix $\mathbf{A}_{\mathrm{S}}$ gives $\mathrm{R_S} \rightarrow \mathrm{N_D}$ additional constraints, which we include as a term $\lambda_{\mathrm{S}} \| \mathbf{A}_{\mathrm{S}}\mathbf{Q}_{\mathrm{H}}\delta\boldsymbol{\Theta} \|^2$ alongside an additional ridge penalty, giving a final

cost function

$$\mathscr{L}(\delta\boldsymbol{\Theta}) = \| \mathbf{F}^{\mathrm{QM/ML}} + \nabla\mathbf{D}^{\mathrm{QM/ML}}[\boldsymbol{\Theta}_0 + \mathbf{Q}_{\mathrm{H}}\delta\boldsymbol{\Theta}]\|^2 + \lambda_{\mathrm{S}}\|\mathbf{A}_{\mathrm{S}}\mathbf{Q}_{\mathrm{H}}\delta\boldsymbol{\Theta}\|^2 + \lambda_0\|\delta\boldsymbol{\Theta}\|^2, \quad (3)$$

where λ_{S} controls the weighting of soft constraints and λ_0 the standard ridge regularization. The minimum criterion $\delta\mathscr{L} = 0$ becomes a linear equation $\mathbf{C}\delta\boldsymbol{\Theta} = \mathbf{y}$, where the matrix $\mathbf{C}$ is always full-rank due to the presence of the ridge term, permitting a direct solution. A Python implementation of this procedure is provided (Code Availability). Via grid search we chose $\lambda_{\mathrm{S}}, \lambda_0$ to yield a mean error of less than 0.015 eV/Å to the soft constraint forces and 0.025 eV/Å to the QM/ML forces, from an initial mean error of nearly 0.2 eV/Å. A detailed presentation of the refitting results are presented in the supplementary materials [58]. We found this balance of hyperparameters controlled against overfitting whilst providing excellent reproduction of energy profiles (via force integration) and relaxed dislocation core structures. Further investigation of increasing potential complexity to further improve the retraining will be the subject of future work. We now apply this method to study dislocation-defect interactions in tungsten.

3. Results

3.1. Dislocation glide in bcc tungsten

In bcc materials screw dislocations with Burgers vector $\mathbf{b} = \frac{1}{2}\langle 111\rangle$ along closed packed $\langle 111\rangle$ directions are the most ubiquitous. Movement of these dislocation is possible in few slip planes [59] with {110} planes being dominant at low temperatures [19,24]. Formation of junction dislocations with Burgers vector along $\langle 100\rangle$ direction occurs as a result reactions of type $\frac{1}{2}[1\bar{1}1] + \frac{1}{2}[11\bar{1}] = [100]$ during strain hardening [60] or plasma exposure [61]. Resulting $\langle 100\rangle$ dislocation can glide in few planes including {001} and {011} depending on the geometry of the reaction [62].

In this section we use an Embedded Atom Method (EAM) potential marked as "EAM2" from Marinica et al. [63], in addition to a recent LML potential from Goryaeva et al. [11] for our application material, tungsten. The LML potential, whose general form is given in Eq. (1), has state-of-the-art accuracy on a wide range of lattice, point defect and screw dislocation properties. These two potentials are employed to calculate the Peierls barriers for junction $\langle 100\rangle$ dislocation in {001} and {011} glide planes. We analyse the performance of the potentials by comparing the results to QM/ML calculations using the LML potential for the embedding ML region, chosen as the LML has perfect matching of the QM elastic constants. Total number of atoms in the cells were 4574 atoms for $[100](00\bar{1})$ model dislocation and 6396 for $[100](011)$ dislocation. While QM/ML mapping consisted of 24 QM and 123 buffer atoms (147 atoms in DFT cluster) for $[100](00\bar{1})$ dislocation and 14 QM and 96 buffer atoms (110 atoms in DFT cluster) for $[100](011)$ dislocation.

Fig. 2 (a, b) show Minimum Energy Paths (MEP) for Peierls barriers calculated with our modified force-only NEB routine (Appendix A). For the {001} glide plane (Fig. 2(a)) the EAM and LML potentials differ significantly both in terms of amplitude and shape of the barrier while for {011} glide plane (Fig. 2(b)) the barriers are practically indistinguishable. Identical results were found using force integration and total energy differences for the NEB routine, again confirming the accuracy of this approach [33]. Both EAM and LML potentials predict the barrier for glide in {001} plane at least three times higher than in {011}. At the same time QM/ML results provide similar values for both glide planes around 0.4 eV. The glide barrier in {001} is overestimated by the potentials while the barrier in {011} is underestimated leading to qualitative disagreement with QM/ML reference data and overall poor performance of the potentials. It is important to note that this work QM/ML barriers are the only available QM reference data for this type of dislocations due to the large size of the simulation cell. Previous work [33,56] has validated and performed extensive convergence checks for the virtual work NEB procedure detailed here.

Access to the QM/ML forces allow us to produce a new LML parametrization using our constrained refitting procedure. The results are shown with green dots and dashed lines in Fig. 2(a,b). The residual force errors of the retrained potential have very little influence on the resulting energy barriers, where an excellent agreement can be seen. We emphasize that the refitting only targeted QM/ML forces, though the resulting LML energetic barriers can be calculated equivalently by force integration or total energy difference.

As the retrained LML potentials closely reproduce dislocation core properties and have essentially perfect matching of elastic constants, they can be used as a highly adaptable embedding medium. We performed QM/ML calculations with a spherical QM region, where the dislocation line crosses the QM/ML boundary (see Figs. 3 and 4(b)), the first time such calculations have been performed to our knowledge. We confirmed that a relaxing a long, straight dislocation in this manner, with a spherical QM region around a small section of the dislocation core, gave no appreciable change in structure, with *maximum* atomic displacement of less than 0.004 Å between the ML and QM regions. In the following sections we exploit this refitting procedure to investigate vacancy segregation to prismatic dislocations, then helium-induced core reconstruction of screw dislocations.

3.2. Dislocation-vacancy segregation energy

The biased diffusion of vacancies to dislocations is the primary source of non-conservative plastic deformation, a critically important process in creep deformation and post-irradiation annealing [2]. Here we look at vacancy segregation at junction $\langle 100\rangle\{011\}$ dislocation as the case study for cross validation of 3D QM/ML coupling procedure against the original LML and a retrained parametrization. We retrained with hard constraints on elastic properties as described above and the vacancy migration pathway, both of which remain in essentially perfect

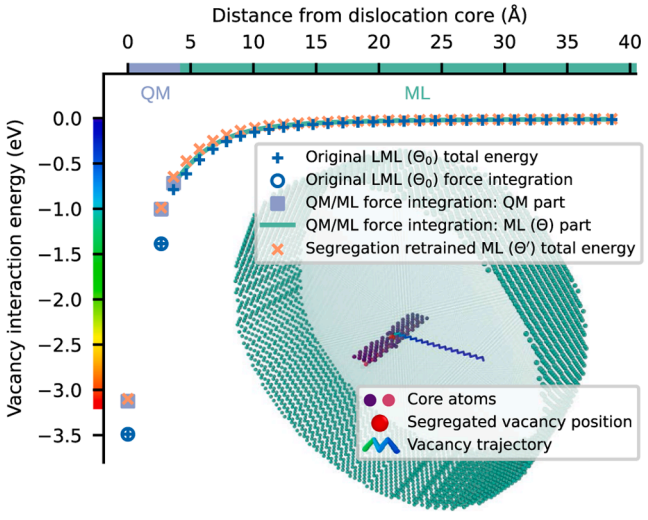

Fig. 3. Energy profile for vacancy segregation to [100](011) edge (also known as junction [64]) dislocation in tungsten calculated with multiple LML potentials and QM/ML force integration [33,56]. The full simulation contained over 70000 atoms, with the vacancy migrating to a spherical QM region. The original LML ($\boldsymbol{\Theta}_0$) potential [11] results demonstrates the force integration procedure exactly agrees with total energy calculations. The QM/ML simulations (for which a total energy does not exist) employed a retrained ML $\boldsymbol{\Theta}$ potential from the NEB path shown in Fig. 2, giving excellent reproduction of the core structure with hard constraints of elastic properties and the vacancy migration. We then further retrained this potential to additionally minimize the error to QM forces from the QM/ML segregation calculation. This final ML $\boldsymbol{\Theta}'$ potential gives excellent prediction of the segregation energy.

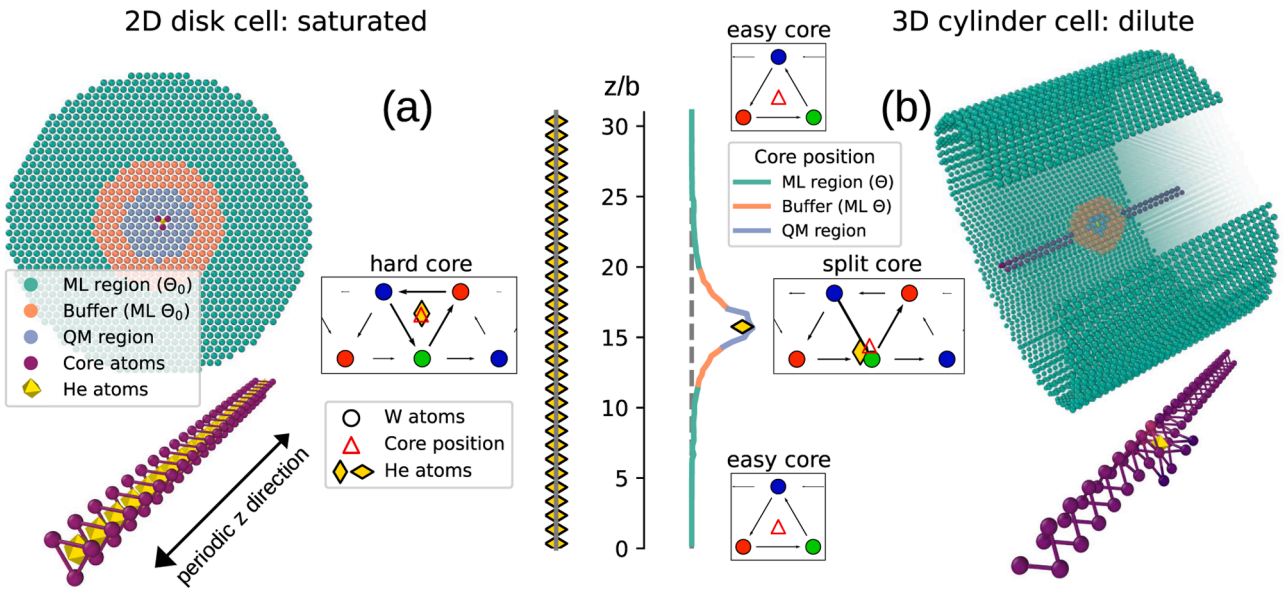

Fig. 4. He-induced reconstruction of screw dislocation core obtained with two simulation geometries. Dislocation core structures are shown using differential displacement maps [65]. (a) An atomic 'disk' of primitive thickness (i.e. a single lattice plane) oriented perpendicular to the dislocation line with a circular QM region centered on the line. This geometry was used for the NEB calculations in Fig. 2. Introduction of He stabilizes the 'hard' core over the 'easy' core, changing the dislocation migration trajectory [24]. (b) A large cylindrical cell orientated along the line direction, with a spherical QM region centered on the He impurity. The He induces a qualitatively different reconstruction to the 'split' core, which slowly relaxes back to the 'easy' core far from the He center. We emphasise that for all the cases the 'Buffer' region is shown purely for descriptive purposes; all atoms in this region are governed by the same LML potential as those in the ML region.

agreement with reference DFT calculations. We confirmed that inclusion of the vacancy migration path in $\mathbf{A}_{\mathrm{H}}$ during the retraining left resulting core structure and Peierls barrier unchanged (Supplementary Materials [58]).

In order to estimate vacancy segregation energy three configurations containing 70355 atoms each with vacancy at increasing distances from the dislocation core were relaxed. After that eleven intermediate configurations between each pair of relaxed configurations were obtained by linear interpolation of atomic positions. A spherical QM region was kept the same for the all the configurations and consisted of the union of spheres centered on the relaxed vacancy positions leading to 27 QM atoms and 351 Buffer atoms (378 atoms in final DFT cell). This large Buffer/QM ratio was chosen to ensure a highly converged solution; however, as we only employ a single k-point the total computational effort is much less than a comparably sized periodic calculation.

The segregation energy was calculated via the virtual work principle, integrating forces along a composite path formed by linearly interpolating minima separated by $\langle 111 \rangle$ jumps, as shown in Fig. 3. Whilst it would be possible to perform NEB relaxations between these minima to additionally obtain migration barriers, this was omitted for computational expediency. The smoothness of the interaction energy across the QM/ML boundary confirms the exceptional matching of dislocation and elastic properties between retrained LML and QM region.

The resulting value of segregation energy estimated by QM/ML approach is 3.1 eV, whilst the original LML potential gives 3.5 eV, demonstrating the reasonable accuracy of this potential even for previously unseen structures. We calculated the segregation energy using both the total energy difference (blue crosses) and virtual work (blue hollow circles). The values for both techniques are identical, serving as a validation for energy difference estimation by virtual work principle.

3.3. Further exploration of the retraining procedure

We further explored the capabilities of the retraining procedure by extending the dislocation glide barrier targets with forces from spherical QM region for three QM/ML relaxed configurations. The resulting segregation retrained potential $\boldsymbol{\Theta}'$ (orange $\times$ marks in Fig. 3) is in excellent agreement to the QM/ML reference result. This demonstrates that the QM/ML retraining procedure detailed here is suitable not only for providing advanced boundary matching but can also be used to qualitatively expand the range of useful training structures for machine learning interatomic potentials, giving systematic improvement.

In order to verify that the constrained retraining ensures that retrained potentials inherit good description of the desired properties we looked at vacancy formation energy, vacancy migration energies and dislocation glide barriers. The results are presented in supplementary materials [58]. It can be seen that both dislocation retrained ($\boldsymbol{\Theta}$) as well as segregation retrained ($\boldsymbol{\Theta}'$) potentials maintain perfect description of elastic properties as well as vacancy behaviour in the bulk. Thus we see no signs of overfitting in the constrained domain.

We note that similar functionality should be achievable with highly flexible (large capacity) approaches employing e.g. neural networks [44,49] or kernels [66] such as GAP [43]. Kernel methods can have theoretically infinite capacity, which is controlled during the refitting procedure by sparsification and providing the relevant information from the database [67]. However, this procedure requires special design of the database, some prior knowledge of relevant atomic configurations for a specific physical problems pointed up with the appropriate theoretical tools [11,68,69]. The present procedure is general and simply requires a linear ML potential with capacity larger than the minimum required for the assimilation of elastic properties. Here, we use a quadratic non-linear ML in descriptors, that can be seen as linear ML potential in an extended descriptor space [11,45]. Moreover, recently, it was shown that this formalism has enough learning capacity in order to assimilate complex features of defects energy landscape in Fe and W [11], thus being appropriate for the present investigation.

3.4. Impurity-induced core reconstruction

In pure tungsten screw $\frac{1}{2}\langle 111 \rangle$ dislocations are characterised by so called 'easy' core [65,70,71] shown by means of differential displacement map in the top and the bottom parts of Fig. 4(b). The glide of screw dislocations is essentially the movement between two equivalent 'easy' core configurations [72]. Point defects segregated on a dislocation line

can affect the relative stability of different core types thus changing the glide mechanism locally. In this section we consider the effect of single helium atom on the core stability of screw dislocation as a challenging application of 3D QM/ML coupling involving foreign atoms in the QM region. The original LML potential has an excellent agreement with DFT for the screw dislocation glide barrier and core structure [11]. The retraining procedure in this case only gave very small adjustments to the original parametrization, which primarily gave small changes in dislocation core structure, with negligible changes in the Peierls barrier. Nevertheless, the retraining procedure was employed to ensure perfect matching for 3D spherical QM region. Importantly, in all cases the DFT region is sufficiently large that no tungsten atoms in the ML region interact directly with the He impurity, only indirectly through induced relaxations. In the general case, where the direct interaction range is larger than the QM region, the ML potential would have to account for the impurity interaction at this range. Whilst we do not anticipate this to arise in most application settings, this will be further investigated in future work.

Figure 4 (a) shows the stabilisation of the 'hard' core by He impurity atom while in pure material this type of core is unstable [24]. These results are obtained using a computational cell containing a one $|\mathbf{b}|$ thick disk of atoms oriented perpendicular to the dislocation line. The cell consists of 1927 atoms with 79 QM atoms shown with blue spheres and 168 buffer atoms shown with orange spheres resulting in a DFT cell containing 247 atoms. Periodic boundary conditions along z direction corresponding to the dislocation line yields in a model quasi infinite dislocation. However, when an impurity atom is added to this cell, it effectively models a dislocation fully decorated with He atoms shown in the bottom of Fig. 4(a). 'Hard' core stabilisation was also seen for the case of carbon in tungsten [26]. Carbon atom occupied a central $\frac{1}{2}|\mathbf{b}|$ position between {111} planes of tungsten atoms forming the hard core. In contrast, stable He position is shifted towards one of the planes with final distance of $\frac{1}{3}|\mathbf{b}|$ to the nearest plane.

Figure 4 (b) shows the results obtained with a cylinder cell composed of 59707 atoms with a spherical QM region centered around the He atom. The resulting DFT cluster contained 396 atoms with 24 atoms in QM region (blue atoms) and 373 atoms in Buffer (orange atoms). The left part of the figure demonstrates the extracted dislocation core position by fitting theoretical displacement field to the atomic displacements extracted from the relaxed atomic positions with $\frac{1}{3}|\mathbf{b}|$ discretisation step [24,26]. It can be seen that the in contrast to 'disk' cell results, He stabilises the 'split' core locally. The dislocation goes back to 'easy' core configuration at distance of $\approx 10\ |\mathbf{b}|$ from the impurity. Similar relaxation lengths were obtained with fully periodic cells for carbon stabilised hard core in tungsten [26]. In this study cells up to $10\ |\mathbf{b}|$ length along dislocation line containing 1350 atoms were considered. The extracted dislocation core position indicated the dislocation does not completely recover the easy core far from the carbon atom even for $10\ |\mathbf{b}|$ cell. This clearly demonstrates that it is essential to have a large cylinder configuration in order to capture effects of point defects on dislocations correctly. It is important to note that carbon atom remained in the same position with increasing the length of the cell while the stabilised core position moved to the middle point on the straight path between hard and easy cores. We obtained significant difference of He atom position between 'disk' and 'cylinder' cells as well as the stabilised split core position largely deviates from the straight easy-hard core path. The absence of jumps of the core position as the dislocation core exits the QM region confirms that we have achieved excellent matching of core properties between QM region and retrained LML potential resulting in a unique simulation tool.

3.5. Helium segregation and hardening

As discussed in the introduction, experiments with helium implanted tungsten show that He concentration as low as 20 appm is sufficient to influence intergranular fracture [17], whilst experiments with much higher concentrations up to $2\times\ 10^5$ appm also demonstrate that TEM-invisible He and He-vacancy clusters can contribute significantly to the resultant hardening [15]. This conclusion is supported by large scale MD simulations of edge and mixed dislocation propagation through these defects [16]. However, the interaction of dislocations with even the most primitive vacancy-helium defects is limited by the accuracy of available interatomic potentials [18], which we address here using our QM/ML methodology.

A number of recent ab initio studies with periodic supercells have parameterized thermodynamic model for impurity segregation to screw dislocations, using segregation models such as (Tréglia et al. [73], equation 23)

$$\frac{C^{\mathrm{He}}_{\mathrm{SD}}}{1-C^{\mathrm{He}}_{\mathrm{SD}}}=\frac{C^{\mathrm{He}}_{\mathrm{bulk}}}{1-C^{\mathrm{He}}_{\mathrm{bulk}}}\exp\left(-\beta\Delta \mathrm{E}^{b}_{He-SD}\right), \tag{4}$$

Segregation of H [74,75] and C [26] in W and in Fe [76,77] were investigated. In the case of W nominal concentrations were in the range of 10–1000 appm and the models are valid only for saturated limit where the dislocation is fully reconstructed to a hard core configuration are considered.

Helium production in transmutation reactions during neutron irradiation is expected to reach levels of 20 appm after 5 years of operation of the DEMO fusion reactor [14]. We use this estimation define the range of nominal concentration of mobile He in the bulk, and study He segregation to screw dislocations. As multiple trapping sites for He will exist, in practice all nominal appm values should be considered an upper bound for the segregation problem, as all He in the material is assumed mobile and available for trapping at screw dislocations. We also neglect He-He interaction, meaning our model is only self-consistent at dilute He concentrations.

To calculate the He binding energy, we first employ the force integration method to give the energy difference between the fully segregated He at the dislocation core (Fig. 5(a)) and a position away from the core (Fig. 5(b)) where the dislocation returns to an almost perfect straight line. This gives an energy difference of $\Delta E^{F}_{\text{He-SD}} = 1.12$ eV.

To obtain a final binding energy we then take the total energy difference $\Delta E^{E}_{\text{He-SD}} = E_{\text{SD}} - E_{\text{He-SD}} + E_{\text{He-bulk}} - E_{\text{bulk}}$, where E_{SD} is the energy of QM cluster with empty screw dislocation, $E^{b}_{\text{He-SD}}$ - energy of QM cluster configuration with He and screw dislocation, E_{bulk} and $E_{\text{He-bulk}}$ - energy of a box with bulk tungsten and same box with He in tetrahedral position. The use of a total energy difference to calculate $\Delta E^{E}_{\text{He-SD}}$ is justified as the He atom in the position shown in Fig. 5(b) induces only minimal dislocation core reconstruction. As a result, the surface of the spherical corresponding QM cluster is very close to the case of empty screw dislocation used as a reference, and thus, the total energy is expected to be a good approximation, as found in other studies [30]. The accuracy of this final approximation will be be verified by further force integration in future work.

This estimation gives the value of $\Delta E^{E}_{\text{He-SD}} = 0.4$ eV resulting in the total He - screw dislocation binding energy of $\Delta E^{b}_{\text{He-SD}} = \Delta E^{F}_{\text{He-SD}} + \Delta E^{E}_{\text{He-SD}} = 1.52$ eV. As can be seen from Fig. 5(d) the applicability of the total energy approximation is also expected to hold for the case of He-vacancy cluster due to the minimal core reconstruction. However, the long range relaxations induced by a vacancy, shown in Fig. 5(c), imply that a total energy difference will not be reliable. In this case, we employ force integration as described in Section 3.2.

The resulting binding energy of He to screw dislocation of 1.52 eV is used in Eq. (4) to provide estimations of the amount of He trapped at dislocations at a range of temperatures (Fig. 6). For ITER divertor operation conditions tungsten monoblocks are expected to heat up to ~2200 K during plasma pulses and cool down to ~900 K between the pulses [78]. Our prediction shown in Fig. 6 indicates that He is segregated on dislocations in the dilute regime during pulses with the

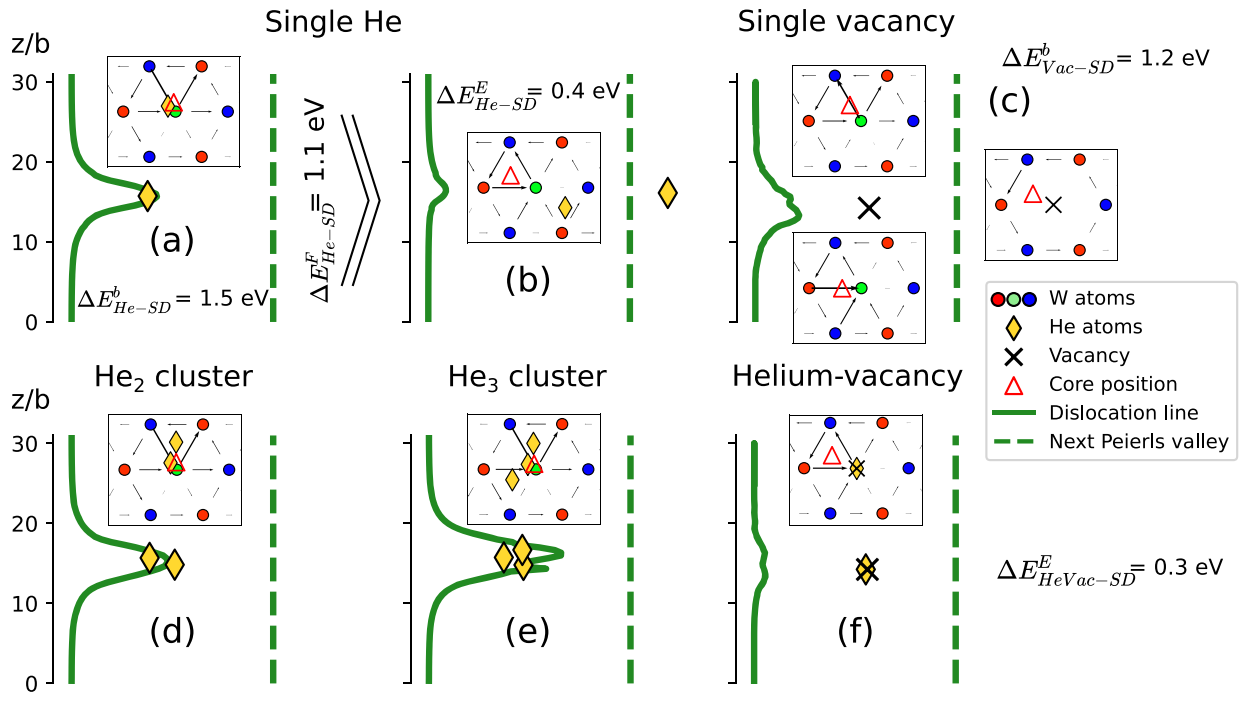

Fig. 5. Reconstruction of screw dislocation core induced by single He atom (a, b), single vacancy (c), He_2 cluster (d), He_3 cluster (e) and helium-vacancy cluster (f). Green solid lines show the extracted dislocation lines, while green dashed lines show the position of next Peierls valley for a straight dislocation in a perfect material. (For interpretation of the references to colour in this figure legend, the reader is referred to the web version of this article.)

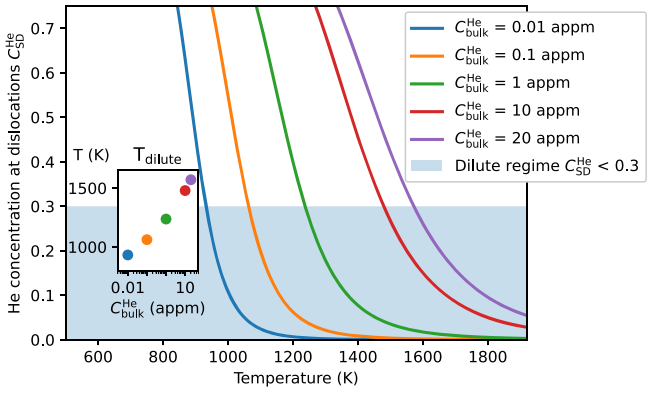

Fig. 6. Concentration of He trapped at screw dislocations assuming binding energy of 1.5 eV. The insert shows the cross over temperature T_{dilute} where concentration of He atoms at screw dislocations $C^{He}_{SD} = 0.3$ indicating the transition between dilute and saturated limits.

transition to the saturated regime between the pulses. To investigate the mechanism of the dilute to saturated transition we performed QM/ML relaxations of He_2 (Fig. 5(d)) and He_3 (Fig. 5(e)) clusters in the same geometry. As can be seen, these clusters did not show stabilisation of hard core even when the saturation is achieved locally. This contrasts with estimation of H [75] and C [26] segregation, which can be expected due to the much higher bulk content and lower temperatures of interest as well as higher binding energies of 2.1 eV for C vs. 1.5 eV for He. Total binding energy estimation of the He interaction energy once trapped at dislocations shows slight repulsion of -0.12 eV for He_2 and -0.16 eV for He_3 clusters. This is to be contrasted with the strong attraction (1 eV) of He in bulk tungsten [79], demonstrating the importance of ab initio calculation of dislocation-defect interactions.

A key element of a recently proposed He hardening mechanism [15] in tungsten is the pinning of screw dislocations by He-vacancy complexes which then bow out into mixed dislocations. To investigate this mechanism we performed a QM/ML relaxation of a single vacancy (Fig. 5(c)) and helium-vacancy complex (He in substitutional position) Fig. 5(f)). The He-vacancy complex shows only a very weak binding energy of 0.3 eV, while vacancy shows signs of core reconstruction with a binding energy of 1.2 eV. As helium clusters can create vacancies by self-trapping mechanism [18,80,81], and vacancies are known to be strong sinks for highly mobile He [82], we can expect the He-vacancy complex to be the dominant point defect [15]. However, our studies show that this gives only a very weak binding energy for screw dislocations, meaning the only plausible hardening mechanism would be a high energetic barrier for bypass. A study of this mechanisms using our QM/ML simulation methodology will be the subject of future work.

4. Conclusions

In this paper, we have shown how state-of-the-art linear machine learning (LML) potentials [11,54] can be used a highly adaptable embedding medium for QM/ML simulations of extended lattice defects, and provided an open source code to allow easy adoption of the method (4). Applying this approach to the calculation of Peierls barriers of ⟨100⟩ edge dislocations revealed much less variation with slip plane compared to current interatomic potentials, with the barrier of ⟨100⟩{010} edge dislocations significantly overestimated, in agreement with previous work [33].

Our new method allows for fully three-dimensional simulation geometries for dislocation-defect interactions, which *qualitatively* change relaxed geometries, as shown in Fig. 4 for He-induced core reconstruction of screw dislocation core in tungsten (Section 3.4).

We emphasize that the largest DFT simulations used in the present work contained less than four hundred atoms, with a single k-point due to the open boundaries. This is approximately equivalent in computational effort to a 128 atom system with a sparse $3 \times 3 \times 3$ k-point grid, a routine calculation in modern theoretical materials science. Due to the general form of retraining procedure and demonstrated applicability of

QM/MM method to grain boundaries [30] and cracks [31], the presented method is generally applicable for any extended defect. Future work will investigate the many opportunities this method offers for the systematic improvement of machine learning potentials, as demonstrated for vacancy-dislocation interactions in Section 3.2.

The method was then applied to the interaction of a range of vacancy-helium defects with dislocations in tungsten and were compared to recent experiments. We found the helium-vacancy defects have a much weaker binding to screw dislocations (0.3 eV) than vacancies alone (1.2 eV) and mobile helium interstitials are predicted to have a mild segregation to screw dislocations at fusion-relevant temperatures. To fully investigate the hardening effects of these defects on $\langle 111 \rangle$ screw dislocations, the primary plasticity carriers in bcc metals, will require simulations of possible bypass mechanisms to ab initio accuracy, which is only possible using the method presented here. This will be subject of a future investigation.

Data availability

Dislocation relaxed configurations, NEB trajectories as well as additional data used for constrained retraining are available at public GitHub repository: https://github.com/marseille-matmol/LML-retrain.

Code availability

The force based QM/MM calculator is available as a part of the `ase.calculators.qmmm` module of the Atomic Simulation Environment (ASE) package [12] as well as the used implementation of preconditioned minimisation algorithms are part of `ase.optimize.precon` module. The tools used to create and analyse atomistic dislocation configurations are available from the `matscipy.dislocation` module [83]. A GitHub repository providing ASE compatible routines to perform the retraining and reproduce all presented results is available at: https://github.com/marseille-matmol/LML-retrain.

Author contributions

PG and TDS designed the study, performed the calculations, derived the constrained retraining procedure and wrote the initial manuscript. All authors participated in discussion and interpretation of the results.

Declaration of Competing Interest

Authors declare that they have no conflict of interest.

Acknowledgements

PG and TDS gratefully recognize support from the Agence Nationale de Recherche, via the MeMoPAS project ANR-19-CE46-0006-1 and the Centre Nationale de Recherce Scientifique, via a Jeunes Entrants grant of the Institut de Physique. This work was granted access to the HPC resources of IDRIS under the allocations A0090910965 and A0120913455 attributed by GENCI and the Computational Simulation Centre of the International Fusion Energy Research Centre in the Rokkasho Fusion Institute of QST (Aomori, Japan), under the Broader Approach grant AbInSeg. This work has been carried out within the framework of the EUROfusion consortium and has received funding from the Euratom research and training programme 2019–2020 under grant agreement no. 633053. AMG, MCM and TDS acknowledge the support from TGCC-CCRT computer centres under the allocation 'Grand Challenge' no. 502 on Topaze. JRK and PG acknowledge support from the UK Engineering and Physical Sciences Research Council (EPSRC) under grant numbers EP/R012474/1 and EP/R043612/1. Additional support was provided by the Leverhulme Trust under grant RPG-2017-191. We are grateful for computational support from the UK national high performance computing service, ARCHER, for which access was obtained via the UKCP consortium and funded by EPSRC grant reference EP/P022065/1. Additional computing facilities were provided by the Scientific Computing Research Technology Platform of the University of Warwick.

Appendix A. QM/ML coupling and energy

Force based QM/ML coupling scheme used here practically requires running two simulations in parallel. In our case we use `LAMMPS` [55] for ML part and `VASP` [84] for DFT cell while the coupling is implemented with python `ASE` interface [12]. The QM/ML forcs $\mathbf{F}_{\mathrm{QM/ML}}$ is obtained by mixing ML force $\mathbf{F}_{\mathrm{LAMMPS}}$ with ab initio force $\mathbf{F}_{\mathrm{VASP}}$ with simple relation:

$$\mathbf{F}_{\mathrm{QM/ML}} = \begin{cases} \mathbf{F}_{\mathrm{VASP}}, & \mathbf{X} \in \mathrm{QM} \\ \mathbf{F}_{\mathrm{LAMMPS}}, & \text{otherwise} \end{cases}, \tag{A.1}$$

where $\mathbf{X}$ is atomic coordinates vector and QM denotes QM region shown with blue color in Fig. 1. The position of the atoms are then updated according to the QM/ML force $\mathbf{F}_{\mathrm{QM/ML}}$ during ionic minimisation. An important aspect of hybrid QM/ML simulations (and open boundary methods more generally) is the need to have a 'buffer' of sacrificial DFT atoms (shown with orange color in Fig. 1), suitably large to protect the target cluster from electronic free surface effects, determined through convergence tests [33]. Here, the positions of buffer atoms are controlled by the ML force $\mathbf{F}_{\mathrm{LAMMPS}}$, as illustrated in Fig. 1. In this way the coupling medium acts as an advanced boundary condition for the `VASP` cell. The size of the QM region depends on the application. For the dislocation glide barrier calculations QM region was centered on the dislocation core and the size was obtained after a series of convergence tests on the glide barrier made in previous works [33,56]. For the spherical QM region centered on a point defect the size was chosen so that the region contains at least two layers of nearest neighbour bulk W atoms.

One well known consequence of this procedure is that as the electronic total energy cannot be partitioned between cluster and buffer, a total energy cannot be defined [32]. However, the ionic (Hellman-Feynmann) forces can be unambiguously assigned, giving a total force vector $\mathbf{F}$ for the system, which has been used to perform structural minimization and dynamics for some time [32]. In recent work [33,56], we have partially lifted this limitation, rigorously extracting energetic *differences* between two configurations through the principle of virtual work. This technique has been implemented in ASE as part of the NEB routine, to compute energies along minimum energy paths. The computational cost of NEB relaxation can be avoided if only end-to-end differences are desired, as demonstrated below when calculating the dislocation-vacancy binding energy, following a linear interpolation between minima. For initial and final atomic configurations $\mathbf{X}_{\mathrm{i,f}}$, we construct some smooth pathway $\mathbf{X}(\lambda)$, where $\lambda \in [0, 1]$ is an affine parameter such that $\mathbf{X}(0) = \mathbf{X}_{\mathrm{i}}$ and $\mathbf{X}(1) = \mathbf{X}_{\mathrm{f}}$, with corresponding ionic forces $\mathbf{F}(\lambda')$. The virtual work energy difference along the pathway then reads [33,56]

$$E(\lambda) - E(0) = \int_0^{\lambda} \mathbf{F}(\lambda') \frac{\mathrm{d}}{\mathrm{d}\lambda'} \mathbf{X}(\lambda') \mathrm{d}\lambda', \tag{A.2}$$

where $(\mathrm{d}/\mathrm{d}\lambda')\mathbf{X}(\lambda')$ is the pathway tangent. If performing a NEB relaxation, $E(\lambda) - E(0)$ will give the minimum energy profile. If the path is an unrelaxed interpolation between two minima, then only the total difference $E(1) - E(0)$ is typically of practical use. Whilst not encountered in the present work, it is possible that a partial relaxation may be beneficial in some settings, to avoid very large forces along the pathway that could cause quadrature issues in Eq. (A.2).

The NEB calculations presented in Fig. 2 evaluated energy barriers from Eq. (A.2), interpolating the eleven intermediate images using a spline interpolation of forces and positions, as detailed in previous work [33,56]. The stopping force tolerance for NEB path optimisation using FIRE algorithm [85] was 0.05 eV/Å. An implementation of our method is provided in the `ASE` simulation package (Code Availability). Starting positions for the NEB relaxation were a obtained by linear interpolation between initial and final configurations relaxed with preconditioned minimisation with adaptive step size selection [86–88] with a maximum force tolerance of 0.01 eV/Å.

Appendix B. DFT parameters

Density functional simulations were performed using `VASP` [84]. The PBE generalised gradient approximation [89] was used to describe effects of electron exchange and correlation together with a projector augmented wave (PAW) basis set with a cut-off energy of 550 eV. Occupancies were smeared with a Methfessel–Paxton scheme of order one with a 0.1 eV smearing width. The Brillouin zone was sampled with a $1 \times 1 \times 12$ Monkhorst-Pack k-point grid for the 2D cluster simulations periodic along the dislocation line and single k-point was used for the calculations with 3D spherical QM regions. The values of these parameters were chosen after a series of convergence tests on forces with a tolerance of few meV/Å.

Appendix C. Linear machine learning potential

We employ a quadratic extension of the bispectral descriptor as implemented in the `MILADY` potential package, first introduced as part of the `SNAP` family of LML potentials [45]. The initial quadratic parametrization used a novel preconditioning procedure as presented in detail in a recent publication [11], to which we refer the reader for further information.

Briefly, let $\mathrm{B}_{ji}(\mathbf{X}), j \in [0, \mathrm{N_B}]$ be the $\mathrm{N_B}$ bispectral components for an atom i, along with a constant component $\mathrm{B}_{0i} \equiv 1$. Only neighboring atoms within the cutoff distance (here 4.7 Å) are included in the descriptor function calculation. The quadratically extended descriptor vector for the system then reads

$$\mathbf{D}(\mathbf{X}) = \sum_i \bigoplus_{j \geq k} \mathrm{B}_{ji}(\mathbf{X}) \mathrm{B}_{ki}(\mathbf{X}) \in \mathbb{R}^{1+2\mathrm{N_B}+{\mathrm{N_B}}^2/2}, \tag{C.1}$$

where $\oplus$ indicates concatenation, giving $(\mathrm{N_B}+1)(\mathrm{N_B}+2)/2 = 1 + 2\mathrm{N_B} + {\mathrm{N_B}}^2/2$ components. The quadratically extended form Eq. (C.1)includes all terms linear in B (terms when $k = 0$). The number of bispectrum components $\mathrm{N_B}$ is determined by an angular moment parameter $j_{\max} = 4$, giving $\mathrm{N_B} = 55$. The original parametrization $\mathbf{\Theta}_0$ is determined in a two stage regression procedure, named 'quadratic noise' [11], where a fit is first found using only the $55 + 1 = 56$ linear combination of bispectrum components, which is then used to precondition a solution employing the above quadratic extension.

Supplementary material

Supplementary material associated with this article can be found, in the online version, at doi:10.1016/j.actamat.2023.118734.

References

[1] J.P. Hirth, J. Lothe, Theory of Dislocations, Malabar, FL Krieger, 1991, https://doi.org/10.1115/1.3167075.

[2] A. Cottrell, An Introduction to Metallurgy, CRC Press, 2019, https://doi.org/10.1201/9780429293917.

[3] A. Argon, Strengthening Mechanisms in Crystal Plasticity vol. 4, Oxford University Press, 2007, https://doi.org/10.1093/acprof:oso/9780198516002.001.0001.

[4] Y.-J. Hu, M.R. Fellinger, B.G. Butler, Y. Wang, K.A. Darling, L.J. Kecskes, D. R. Trinkle, Z.-K. Liu, Solute-induced solid-solution softening and hardening in bcc tungsten, Acta Mater. 141 (2017) 304–316, https://doi.org/10.1016/j.actamat.2017.09.019.

[5] S. Zinkle, G. Was, Materials challenges in nuclear energy, Acta Mater. 61 (3) (2013) 735–758, https://doi.org/10.1016/j.actamat.2012.11.004.

[6] R.-Y. Zheng, W.-R. Jian, I.J. Beyerlein, W.-Z. Han, Atomic-scale hidden point-defect complexes induce ultrahigh-irradiation hardening in tungsten, Nano Lett. 21 (13) (2021) 5798–5804, https://doi.org/10.1021/acs.nanolett.1c01637.

[7] C. Varvenne, G. Leyson, M. Ghazisaeidi, W. Curtin, Solute strengthening in random alloys, Acta Mater. 124 (2017) 660–683, https://doi.org/10.1016/j.actamat.2016.09.046.

[8] S. Nag, W.A. Curtin, Effect of solute-solute interactions on strengthening of random alloys from dilute to high entropy alloys, Acta Mater. 200 (2020) 659–673, https://doi.org/10.1016/j.actamat.2020.08.011.

[9] M. Gilbert, K. Arakawa, Z. Bergstrom, M. Caturla, S. Dudarev, F. Gao, A. Goryaeva, S. Hu, X. Hu, R. Kurtz, A. Litnovsky, J. Marian, M.-C. Marinica, E. Martinez, E. Marquis, D. Mason, B. Nguyen, P. Olsson, Y. Osetskiy, D. Senor, W. Setyawan, M. Short, T. Suzudo, J. Trelewicz, T. Tsuru, G. Was, B. Wirth, L. Yang, Y. Zhang, S. Zinkle, Perspectives on multiscale modelling and experiments to accelerate materials development for fusion, J. Nucl. Mater. 554 (2021) 153113, https://doi.org/10.1016/j.jnucmat.2021.153113.

[10] R.M. Martin, Electronic Structure, Cambridge University Press, 2004, https://doi.org/10.1017/cbo9780511805769.

[11] A.M. Goryaeva, J. Dérès, C. Lapointe, P. Grigorev, T.D. Swinburne, J.R. Kermode, L. Ventelon, J. Baima, M.-C. Marinica, Efficient and transferable machine learning potentials for the simulation of crystal defects in bcc Fe and W, Phys. Rev. Mater. 5 (10) (2021) 103803, https://doi.org/10.1103/physrevmaterials.5.103803.

[12] A. Hjorth Larsen, J. Jørgen Mortensen, J. Blomqvist, I.E. Castelli, R. Christensen, M. Dułak, J. Friis, M.N. Groves, B. Hammer, C. Hargus, E.D. Hermes, P.C. Jennings, P. Bjerre Jensen, J. Kermode, J.R. Kitchin, E. Leonhard Kolsbjerg, J. Kubal, K. Kaasbjerg, S. Lysgaard, J. Bergmann Maronsson, T. Maxson, T. Olsen, L. Pastewka, A. Peterson, C. Rostgaard, J. Schiøtz, O. Schütt, M. Strange, K. S. Thygesen, T. Vegge, L. Vilhelmsen, M. Walter, Z. Zeng, K.W. Jacobsen, The atomic simulation environment—A python library for working with atoms, J. Phys. 29 (27) (2017) 273002, https://doi.org/10.1088/1361-648x/aa680e.

[13] P. Grigorev, T.D. Swinburne, LML constrained retraining package, 2021, https://github.com/marseille-matmol/LML-retrain.

[14] M. Gilbert, S. Dudarev, S. Zheng, L. Packer, J.-C. Sublet, An integrated model for materials in a fusion power plant: transmutation, gas production, and helium embrittlement under neutron irradiation, Nucl. Fusion 52 (8) (2012) 083019, https://doi.org/10.1088/0029-5515/52/8/083019.

[15] R.-Y. Zheng, W.-R. Jian, I.J. Beyerlein, W.-Z. Han, Atomic-scale hidden point-defect complexes induce ultrahigh-irradiation hardening in tungsten, Nano Lett. 21 (13) (2021) 5798–5804, https://doi.org/10.1021/acs.nanolett.1c01637.PMID: 34228459

[16] Q.-Y. Ren, Y.-H. Li, N. Gao, W.-Z. Han, Y.-Z. Niu, H.-X. Xie, Y. Zhang, F. Gao, G.-H. Lu, H.-B. Zhou, Revealing the synergistic effect of invisible helium clusters in helium irradiation hardening in tungsten, Scr. Mater. 219 (2022) 114850, https://doi.org/10.1016/j.scriptamat.2022.114850.

[17] T. Miyazawa, T. Hwang, K. Tsuchida, T. Hattori, M. Fukuda, S. Nogami, A. Hasegawa, Effects of helium on mechanical properties of tungsten for fusion applications, Nucl. Mater. Energy 15 (2018) 154–157, https://doi.org/10.1016/j.nme.2018.04.003.

[18] G. Bonny, D. Terentyev, A. Bakaev, P. Grigorev, D. Van Neck, Many-body central force potentials for tungsten, Model. Simul. Mater. Sci. Eng. 22 (5) (2014) 053001, https://doi.org/10.1088/0965-0393/22/5/053001.

[19] E. Clouet, B. Bienvenu, L. Dezerald, D. Rodney, Screw dislocations in BCC transition metals: from ab initio modeling to yield criterion, C. R. Phys. 22 (S3) (2021) 83–116, https://doi.org/10.5802/crphys.75.

[20] C. Woodward, First-principles simulations of dislocation cores, Mater. Sci. Eng. 400–401 (2005) 59–67, https://doi.org/10.1016/j.msea.2005.03.039.

[21] L. Ventelon, F. Willaime, Core structure and peierls potential of screw dislocations in α-Fe from first principles: cluster versus dipole approaches, J. Computer-Aided Mater. Des. 14 (S1) (2007) 85–94, https://doi.org/10.1007/s10820-007-9064-y.

[22] D. Rodney, L. Ventelon, E. Clouet, L. Pizzagalli, F. Willaime, Ab initio modeling of dislocation core properties in metals and semiconductors, Acta Mater. 124 (2017) 633–659, https://doi.org/10.1016/j.actamat.2016.09.049.

[23] L. Dezerald, L. Proville, L. Ventelon, F. Willaime, D. Rodney, First-principles prediction of kink-pair activation enthalpy on screw dislocations in bcc transition metals: V, Nb, Ta, Mo, W, and Fe, Phys. Rev. B 91 (9) (2015) 094105, https://doi.org/10.1103/physrevb.91.094105.

[24] L. Dezerald, D. Rodney, E. Clouet, L. Ventelon, F. Willaime, Plastic anisotropy and dislocation trajectory in BCC metals, Nat. Commun. 7 (1) (2016) 11695, https://doi.org/10.1038/ncomms11695.

[25] E. Clouet, D. Caillard, N. Chaari, F. Onimus, D. Rodney, Dislocation locking versus easy glide in titanium and zirconium, Nat. Mater. 14 (9) (2015) 931–936, https://doi.org/10.1038/nmat4340.

[26] G. Hachet, L. Ventelon, F. Willaime, E. Clouet, Screw dislocation-carbon interaction in BCC tungsten: an ab initio study, Acta Mater. 200 (2020) 481–489, https://doi.org/10.1016/j.actamat.2020.09.014.

[27] C. Woodward, S.I. Rao, Flexible ab initio boundary conditions: simulating isolated dislocations in bcc Mo and Ta, Phys. Rev. Lett. 88 (21) (2002) 216402, https://doi.org/10.1103/physrevlett.88.216402.

[28] M.R. Fellinger, A.M.Z. Tan, L.G. Hector, D.R. Trinkle, Geometries of edge and mixed dislocations in bcc Fe from first-principles calculations, Phys. Rev. Mater. 2 (11) (2018) 113605, https://doi.org/10.1103/physrevmaterials.2.113605.

[29] G.P.M. Leyson, W.A. Curtin, L.G. Hector, C.F. Woodward, Quantitative prediction of solute strengthening in aluminium alloys, Nat. Mater. 9 (9) (2010) 750–755, https://doi.org/10.1038/nmat2813.

[30] M. Wagih, C.A. Schuh, Learning grain-boundary segregation: from first principles to polycrystals, Phys. Rev. Lett. 129 (4) (2022) 046102, https://doi.org/10.1103/physrevlett.129.046102.

[31] J.R. Kermode, T. Albaret, D. Sherman, N. Bernstein, P. Gumbsch, M.C. Payne, G. Csányi, A. De Vita, Low-speed fracture instabilities in a brittle crystal, Nature 455 (7217) (2008) 1224–1227, https://doi.org/10.1038/nature07297.

[32] N. Bernstein, J.R. Kermode, G. Csányi, Hybrid atomistic simulation methods for materials systems, Rep. Prog. Phys. 72 (2) (2009) 026501, https://doi.org/10.1088/0034-4885/72/2/026501.

[33] T.D. Swinburne, J.R. Kermode, Computing energy barriers for rare events from hybrid quantum/classical simulations through the virtual work principle, Phys. Rev. B 96 (14) (2017) 144102, https://doi.org/10.1103/physrevb.96.144102.

[34] J. Shao, Linear model selection by cross-validation, J. Am. Stat. Assoc. 88 (422) (1993) 486–494, https://doi.org/10.1080/01621459.1993.10476299.

[35] N. Srivastava, G. Hinton, A. Krizhevsky, I. Sutskever, R. Salakhutdinov, Dropout: a simple way to prevent neural networks from overfitting, J. Mach. Learn. Res. 15 (1) (2014) 1929–1958.

[36] D.J.C. MacKay, Bayesian interpolation, Neural Comput. 4 (3) (1992) 415–447, https://doi.org/10.1162/neco.1992.4.3.415.

[37] A.M. Goryaeva, J.-B. Maillet, M.-C. Marinica, Towards better efficiency of interatomic linear machine learning potentials, Comput. Mater. Sci. 166 (2019) 200–209, https://doi.org/10.1016/j.commatsci.2019.04.043.

[38] V.L. Deringer, A.P. Bartók, N. Bernstein, D.M. Wilkins, M. Ceriotti, G. Csányi, Gaussian process regression for materials and molecules, Chem. Rev. 121 (16) (2021) 10073–10141, https://doi.org/10.1021/acs.chemrev.1c00022.

[39] Y. Mishin, Machine-learning interatomic potentials for materials science, Acta Mater. 214 (2021) 116980, https://doi.org/10.1016/j.actamat.2021.116980.

[40] B. Onat, C. Ortner, J.R. Kermode, Sensitivity and dimensionality of atomic environment representations used for machine learning interatomic potentials, J. Chem. Phys. 153 (14) (2020) 144106, https://doi.org/10.1063/5.0016005.

[41] O.T. Unke, S. Chmiela, H.E. Sauceda, M. Gastegger, I. Poltavsky, K.T. Schütt, A. Tkatchenko, K.-R. Müller, Machine learning force fields, Chem. Rev. 121 (16) (2021) 10142–10186, https://doi.org/10.1021/acs.chemrev.0c01111.

[42] A.P. Bartók. Gaussian Approximation Potential : An Interatomic Potential Derived from First Principles Quantum Mechanics, University of Cambridge, 2009. Ph.D. thesis.

[43] A.P. Bartók, M.C. Payne, R. Kondor, G. Csányi, Gaussian approximation potentials: the accuracy of quantum mechanics, without the electrons, Phys. Rev. Lett. 104 (13) (2010) 136403, https://doi.org/10.1103/physrevlett.104.136403.

[44] J. Behler, M. Parrinello, Generalized neural-network representation of high-dimensional potential-energy surfaces, Phys. Rev. Lett. 98 (14) (2007) 146401, https://doi.org/10.1103/physrevlett.98.146401.

[45] A. Thompson, L. Swiler, C. Trott, S. Foiles, G. Tucker, Spectral neighbor analysis method for automated generation of quantum-accurate interatomic potentials, J. Comput. Phys. 285 (2015) 316–330, https://doi.org/10.1016/j.jcp.2014.12.018.

[46] A.V. Shapeev, Moment tensor potentials: a class of systematically improvable interatomic potentials, Multiscale Model. Simul. 14 (3) (2016) 1153–1173, https://doi.org/10.1137/15m1054183.

[47] E.V. Podryabinkin, A.V. Shapeev, Active learning of linearly parametrized interatomic potentials, Comput. Mater. Sci. 140 (2017) 171–180, https://doi.org/10.1016/j.commatsci.2017.08.031.

[48] A.E.A. Allen, G. Dusson, C. Ortner, G. Csányi, Atomic permutationally invariant polynomials for fitting molecular force fields, Mach. Learn. 2 (2) (2021) 025017, https://doi.org/10.1088/2632-2153/abd51e.

[49] G.P.P. Pun, R. Batra, R. Ramprasad, Y. Mishin, Physically informed artificial neural networks for atomistic modeling of materials, Nat. Commun. 10 (1) (2019), https://doi.org/10.1038/s41467-019-10343-5.

[50] S. Chmiela, H.E. Sauceda, K.-R. Müller, A. Tkatchenko, Towards exact molecular dynamics simulations with machine-learned force fields, Nat. Commun. 9 (1) (2018) 1–10, https://doi.org/10.1038/s41467-018-06169-2.

[51] Y. Lysogorskiy, C.v.d. Oord, A. Bochkarev, S. Menon, M. Rinaldi, T. Hammerschmidt, M. Mrovec, A. Thompson, G. Csányi, C. Ortner, R. Drautz, Performant implementation of the atomic cluster expansion (PACE) and application to copper and silicon, npj Comput. Mater. 7 (1) (2021) 1–12, https://doi.org/10.1038/s41524-021-00559-9.

[52] R. Drautz, Atomic cluster expansion for accurate and transferable interatomic potentials, Phys. Rev. B 99 (1) (2019) 014104, https://doi.org/10.1103/physrevb.99.014104.

[53] R. Drautz, Atomic cluster expansion of scalar, vectorial, and tensorial properties including magnetism and charge transfer, Phys. Rev. B 102 (2) (2020) 024104, https://doi.org/10.1103/physrevb.102.024104.

[54] A.M. Goryaeva, C. Lapointe, T.D. Swinburne, M.-C. Marinica, Lammps-MiLaDy package, 2021, https://github.com/ai-atoms/Lammps-MiLaDy.

[55] A.P. Thompson, H.M. Aktulga, R. Berger, D.S. Bolintineanu, W.M. Brown, P. S. Crozier, P.J. in 't Veld, A. Kohlmeyer, S.G. Moore, T.D. Nguyen, R. Shan, M. J. Stevens, J. Tranchida, C. Trott, S.J. Plimpton, LAMMPS—A flexible simulation tool for particle-based materials modeling at the atomic, meso, and continuum scales, Comput. Phys. Commun. 271 (2022) 108171, https://doi.org/10.1016/j.cpc.2021.108171.

[56] P. Grigorev, T.D. Swinburne, J.R. Kermode, Hybrid quantum/classical study of hydrogen-decorated screw dislocations in tungsten: ultrafast pipe diffusion, core reconstruction, and effects on glide mechanism, Phys. Rev. Mater. 4 (2) (2020) 023601, https://doi.org/10.1103/physrevmaterials.4.023601.

[57] G. Strang, Introduction to Linear Algebra vol. 3, Wellesley-Cambridge Press Wellesley, MA, 1993.

[58] P. Grigorev, A.M. Goryaeva, J.R. Kermode, M.-C. Marinica, T.D. Swinburne, Supplementary materials, 2022.

[59] C.R. Weinberger, B.L. Boyce, C.C. Battaile, Slip planes in bcc transition metals, Int. Mater. Rev. 58 (5) (2013) 296–314, https://doi.org/10.1179/1743280412y.0000000015.

[60] V.V. Bulatov, L.L. Hsiung, M. Tang, A. Arsenlis, M.C. Bartelt, W. Cai, J.N. Florando, M. Hiratani, M. Rhee, G. Hommes, T.G. Pierce, T.D. de la Rubia, Dislocation multi-junctions and strain hardening, Nature 440 (7088) (2006) 1174–1178, https://doi.org/10.1038/nature04658.

[61] W. Guo, L. Ge, Y. Yuan, L. Cheng, S. Wang, X. Zhang, G.-H. Lu, $\langle 0\,0\,1\rangle$ edge dislocation nucleation mechanism of surface blistering in tungsten exposed to deuterium plasma, Nucl. Fusion 59 (2) (2018) 026005, https://doi.org/10.1088/1741-4326/aaf32e.

[62] N. Bertin, W. Cai, S. Aubry, V.V. Bulatov, Core energies of dislocations in bcc metals, Phys. Rev. Mater. 5 (2) (2021), https://doi.org/10.1103/physrevmaterials.5.025002.

[63] M.-C. Marinica, L. Ventelon, M.R. Gilbert, L. Proville, S.L. Dudarev, J. Marian, G. Bencteux, F. Willaime, Interatomic potentials for modelling radiation defects and dislocations in tungsten, J. Phys. 25 (39) (2013) 395502, https://doi.org/10.1088/0953-8984/25/39/395502.

[64] N. Bertin, W. Cai, S. Aubry, V.V. Bulatov, Core energies of dislocations in bcc metals, Phys. Rev. Mater. 5 (2) (2021) 025002, https://doi.org/10.1103/physrevmaterials.5.025002.

[65] V. Vitek, Theory of the core structures of dislocations in BCC metals, Cryst. Latt. Def. Amorph. 5 (1668) (1974) 1–34.

[66] C.E. Rasmussen, Gaussian Processes in Machine Learning, Springer, Berlin, Heidelberg, 2004, https://doi.org/10.1007/978-3-540-28650-9_4.

[67] N. Bernstein, G. Csányi, V.L. Deringer, De novo exploration and self-guided learning of potential-energy surfaces, npj Comput. Mater. 5 (1) (2019) 99, https://doi.org/10.1038/s41524-019-0236-6.

[68] A.P. Bartók, S. De, C. Poelking, N. Bernstein, J.R. Kermode, G. Csányi, M. Ceriotti, Machine learning unifies the modeling of materials and molecules, Sci. Adv. 3 (12) (2017) e1701816, https://doi.org/10.1126/sciadv.1701816.

[69] A.M. Goryaeva, C. Lapointe, C. Dai, J. Dérès, J.-B. Maillet, M.-C. Marinica, Reinforcing materials modelling by encoding the structures of defects in crystalline solids into distortion scores, Nat. Commun. 11 (1) (2020) 1–14, https://doi.org/10.1038/s41467-020-18282-2.

[70] S. Takeuchi, Core structure of a screw dislocation in the b.c.c. lattice and its relation to slip behaviour of α-iron, Philos. Mag. A 39 (5) (1979) 661–671, https://doi.org/10.1080/01418617908239296.

[71] W. Cai, V.V. Bulatov, J. Chang, J. Li, S. Yip, Dislocation core effects on mobility, in: F. Nabarro, J. Hirth (Eds.), Dislocations in Solids, Dislocations in Solids, vol. 12, Elsevier, 2004, pp. 1–80, https://doi.org/10.1016/s1572-4859(05)80003-8.
[72] L. Ventelon, F. Willaime, E. Clouet, D. Rodney, Ab initio investigation of the peierls potential of screw dislocations in bcc Fe and W, Acta Mater. 61 (11) (2013) 3973–3985, https://doi.org/10.1016/j.actamat.2013.03.012.
[73] G. Tréglia, B. Legrand, F. Ducastelle, A. Saúl, C. Gallis, I. Meunier, C. Mottet, A. Senhaji, Alloy surfaces: segregation, reconstruction and phase transitions, Comput. Mater. Sci. 15 (2) (1999) 196–235, https://doi.org/10.1016/s0927-0256(99)00004-x.
[74] P.P. Borges, E. Clouet, L. Ventelon, Ab initio investigation of the screw dislocation-hydrogen interaction in bcc tungsten and iron, Acta Mater. 234 (2022) 118048, https://doi.org/10.1016/j.actamat.2022.118048.
[75] Y.-H. Li, H.-B. Zhou, F. Gao, G. Lu, G.-H. Lu, F. Liu, Hydrogen induced dislocation core reconstruction in bcc tungsten, Acta Mater. 226 (2022) 117622, https://doi.org/10.1016/j.actamat.2022.117622.
[76] M. Itakura, H. Kaburaki, M. Yamaguchi, T. Okita, The effect of hydrogen atoms on the screw dislocation mobility in bcc iron: a first-principles study, Acta Mater. 61 (18) (2013) 6857–6867, https://doi.org/10.1016/j.actamat.2013.07.064.
[77] L. Ventelon, B. Lüthi, E. Clouet, L. Proville, B. Legrand, D. Rodney, F. Willaime, Dislocation core reconstruction induced by carbon segregation in bcc iron, Phys. Rev. B 91 (22) (2015) 220102(R), https://doi.org/10.1103/physrevb.91.220102.
[78] T. Hirai, S. Panayotis, V. Barabash, C. Amzallag, F. Escourbiac, A. Durocher, M. Merola, J. Linke, T. Loewenhoff, G. Pintsuk, M. Wirtz, I. Uytdenhouwen, Use of tungsten material for the ITER divertor, Nucl. Mater. Energy 9 (2016) 616–622, https://doi.org/10.1016/j.nme.2016.07.003.
[79] C.S. Becquart, C. Domain, Migration energy of He in W revisited by ab initio calculations, Phys. Rev. Lett. 97 (19) (2006) 196402, https://doi.org/10.1103/physrevlett.97.196402.
[80] J. Boisse, C. Domain, C. Becquart, Modelling self trapping and trap mutation in tungsten using DFT and molecular dynamics with an empirical potential based on DFT, J. Nucl. Mater. 455 (1–3) (2014) 10–15, https://doi.org/10.1016/j.jnucmat.2014.02.031.Proceedings of the 16th International Conference on Fusion Reactor Materials (ICFRM-16)
[81] P. Grigorev, A. Zinovev, D. Terentyev, G. Bonny, E.E. Zhurkin, G. Van Oost, J.-M. Noterdaeme, Molecular dynamics simulation of hydrogen and helium trapping in tungsten, J. Nucl. Mater. 508 (2018) 451–458, https://doi.org/10.1016/j.jnucmat.2018.05.052.
[82] C. Becquart, C. Domain, A density functional theory assessment of the clustering behaviour of He and H in tungsten, J. Nucl. Mater. 386–388 (2009) 109–111, https://doi.org/10.1016/j.jnucmat.2008.12.085.
[83] J.R. Kermode, L. Pastewka, P. Grigorev, Matscipy: generic python materials science toolkit, 2020, https://github.com/libAtoms/matscipy.
[84] G. Kresse, J. Furthmüller, Efficient iterative schemes for ab initio total-energy calculations using a plane-wave basis set, Phys. Rev. B 54 (16) (1996) 11169–11186, https://doi.org/10.1103/physrevb.54.11169.
[85] E. Bitzek, P. Koskinen, F. Gähler, M. Moseler, P. Gumbsch, Structural relaxation made simple, Phys. Rev. Lett. 97 (17) (2006) 170201, https://doi.org/10.1103/physrevlett.97.170201.
[86] D. Packwood, J. Kermode, L. Mones, N. Bernstein, J. Woolley, N. Gould, C. Ortner, G. Csányi, A universal preconditioner for simulating condensed phase materials, J. Chem. Phys. 144 (16) (2016) 164109, https://doi.org/10.1063/1.4947024.
[87] L. Mones, C. Ortner, G. Csányi, Preconditioners for the geometry optimisation and saddle point search of molecular systems, Sci. Rep. 8 (1) (2018) 1–11, https://doi.org/10.1038/s41598-018-32105-x.
[88] S. Makri, C. Ortner, J.R. Kermode, A preconditioning scheme for minimum energy path finding methods, J. Chem. Phys. 150 (9) (2019) 094109, https://doi.org/10.1063/1.5064465.
[89] J.P. Perdew, K. Burke, M. Ernzerhof, Generalized gradient approximation made simple, Phys. Rev. Lett. 77 (18) (1996) 3865–3868, https://doi.org/10.1103/physrevlett.77.3865.